Immiscibility in binary silicate liquids: Insight from *ab initio* molecular dynamics simulations

Xuan Ge,[1,2] Pingsheng Lai,[1] Caijuan Shi,[3] Tao Du,[2] Zhencai Li,[2] Wenquan Lu,[1] Jingyu Qin,[4] Fan Yang,[5] Yuanzheng Yue,[2] Morten M. Smedskjaer,[2,*] Jianguo Li,[1] and Qiaodan Hu[1,†]

[1]*Shanghai Key Laboratory of Materials Laser Processing and Modification, School of Materials Science and Engineering, Shanghai Jiao Tong University, 200240 Shanghai, China*

[2]*Department of Chemistry and Bioscience, Aalborg University, 9220 Aalborg, Denmark*

[3]*Beijing Synchrotron Radiation Facility, Institute of High Energy Physics, Chinese Academy of Sciences, 100049 Beijing, China*

[4]*School of Materials Science and Engineering, Shandong University, 250100 Jinan, China*

[5]*School of Mechanical Engineering, Shanghai Jiao Tong University, 200240 Shanghai, China*

(Received 28 March 2024; revised 7 May 2024; accepted 10 May 2024; published 31 May 2024)

Liquid-liquid phase separation (LLPS) is a prevalent phenomenon in silicate liquids. The ionic potential of the cations is widely recognized as a pivotal factor controlling the immiscibility extent of silicates; nonetheless, the intricate relationship between the two has yet to be fully understood. Here, using *ab initio* molecular dynamics simulations, we study the static and dynamic structural evolutions in a prototypical LLPS system (TiO_2-SiO_2), aiming to decode the structural origin of the nonmonotonic dependence of ionic potential on immiscibility extent. The simulations reproduce the initial stage of phase separation as represented by formation of microscale aggregative Ti-Ti clusters upon cooling. Such microphase separation primarily arises from the Coulombic repulsion between Ti^{4+} cations and adjacent Si^{4+} nodes, rather than the previously believed repulsion between poorly shielded Ti^{4+} cations. Analysis of dynamics reveals that the transport of Ti^{4+} cations across the Si-O-Si network is more sluggish than that of alkali (alkaline)-earth cations. Slow dynamics of Ti^{4+} cations are decoupled from their local coordination structure, but instead, it highly depends on the topological rigidity of these nearest-neighbor Ti–O bonds. As such, the high ionic potential of Ti^{4+} cations drives them away from nearby-network Si^{4+} nodes, promoting immiscibility. On the other hand, this same potential causes strong topological rigidity, and hence, suppresses immiscibility by hindering the Ti^{4+} migration. This dual effect of the ionic potential questions the classical structural model in LLPS and provides insights into the association between immiscibility extent and ionic potential.

DOI: 10.1103/PhysRevB.109.174215

I. INTRODUCTION

Liquid immiscibility, also known as liquid-liquid phase separation (LLPS), creates mesoscopic heterogeneity in materials and plays a critical role both in nature and industrial applications, including minerals formation in deposits [1,2], generation of membraneless compartments in cells [3], and synthesis of functional materials with heterogeneous structure [4,5]. Usually, in glass manufacturing, it is desirable to prevent the occurrence of liquid immiscibility, since the difference in refractive index between the different glassy phases may degrade the optical transparency [6]. Moreover, the interface between the two phases can act as the preferred site for crystal nucleation [7]. However, recently some studies have illustrated that the mechanical and optical properties of glasses could be effectively optimized by controlling the size and distribution of heterogeneous phases [8–10]. To suppress or promote LLPS depending on the application requires a determination of the size of the immiscibility region; that is, the extent of immiscibility for given compositions.

The extent of immiscibility, including compositional extents (the compositional range of two-liquid regions) and thermal extent (the temperature gap between consolute temperature and liquidus temperature), has been studied using thermodynamic models. The subregular solution model serves as the foundation for understanding LLPS. It involves the excess free-energy term ΔG^{E} and can reproduce asymmetric miscibility gaps observed in various material systems, including metallic and silicate glass-forming liquids [11,12]. However, employing thermodynamic models to study liquid immiscibility has some inherent limitations: (i) The unknown interactions between the chemical components make the determination of ΔG^{E} always empirical [13]. Rigorous thermodynamic solutions are limited to a finite equilibrium system; and (ii) Complex many-body effects among the components and the weak transferability of fitted interaction parameters across different systems render the thermodynamic modeling of ternary and multicomponent systems exceptionally challenging [14].

Unveiling the structural origins of liquid immiscibility provides a fundamental solution for determining the

*Corresponding author: mos@bio.aau.dk
†Corresponding author: qdhu@sjtu.edu.cn

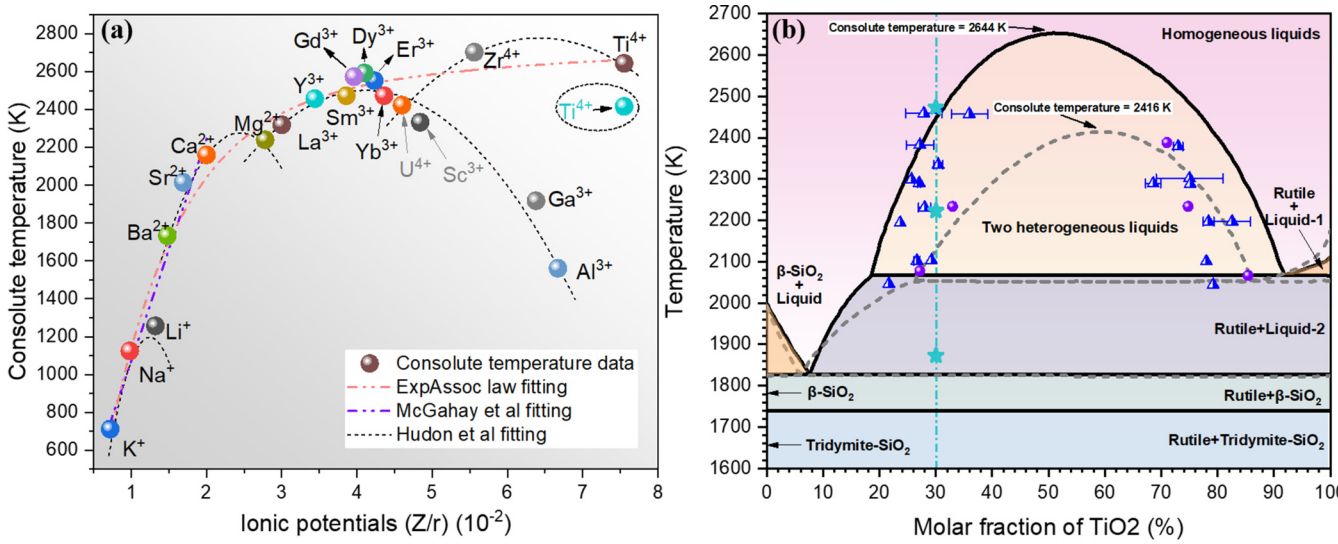

FIG. 1. (a) Consolute temperature of liquid immiscibility in binary silicate systems as a function of the ionic potential of foreign cations. As the ionic potential increases, the consolute temperature negatively deviates from linearity (McGahay *et al.* fitting [21]), and a nonlinear curve (ExpAssoc law, dashed-dotted-dotted line) was employed to visually fit such relationship. The parabolic fitting curves correspond to Hudon's selective-solute model [22], where a group of cations with the same chemical valence are fitted together. (b) Phase diagram of SiO_2-TiO_2 system. Phase region boundaries indicated by solid black lines are referenced from the work of DeCapitani and Kirschen [30]. Meanwhile, their experimental composition-temperature points determining the LLPS dome are also plotted in the phase diagram as blue triangles. The immiscibility region determined by Kirillova *et al.* is indicated by gray dashed lines, which were obtained by fitting experimental results (denoted as purple spheres) [29]. The composition and temperatures considered in this work are represented by a vertical dashed-dotted line and star symbols, respectively.

immiscibility extent in complicated systems. Warren and Pincus proposed that the competition between network formers and network modifiers for nonbridging oxygen (to maintain charge balance) led to liquid immiscibility [15]. Based on this principle, they inferred that the immiscibility extent was mainly influenced by two critical factors: the random separated distance between the neighbored modifying cations (d_0) and the ionic potential (Z/r, where Z is valence and r is the radius) of the modifying cations. Such inference was further verified by Levin and Block, who utilized the geometric constraints (i.e., d_0) to calculate the compositional extent of LLPS in binary silicate and ternary borosilicate liquids. The calculated results are in good agreement with the experimental ones [16,17]. Despite this progress, these structural parameters cannot comprehensively portray the immiscibility extent. As shown in Fig. 1, the consolute temperatures in binary silicates do not show a direct proportional increase with an increase in ionic potential. Instead, they exhibit a nonlinear and nonmonotonical change when extrapolating to larger ionic potentials beyond those observed in alkali (alkaline)-earth silicates. Additionally, the consolute temperature of certain specific cations, such as Al^{3+}, Ti^{4+}, and Ga^{3+}, strongly deviates from the trend derived from alkali (alkaline)-earth silicates, manifesting a notable reduction in their thermal externs of immiscibility. To explain these observed deviations. Varshal *et al.* attributed the reduced consolute temperature of Al^{3+} to the compatibility between similar structural groups (e.g., $[AlO_4]$ and $[SiO_4]$ units) [18]. Indeed, this concept of "structural compatibility" has been corroborated by diffraction results [19,20], but it fails to be used for calculating the immiscibility extent. McGahay and Tomozawa postulated that the silicate liquids were driven toward separation by strong Coulombic repulsion between poorly shielding modifier cations. By describing repulsion interactions using the Debye-Hückel electrolyte theory, they derived a linear relationship between ionic potential and consolute temperature, as presented in the purple double-dashed line in Fig. 1 [21]. This relationship explains the variation of consolute temperature vs ionic potential well in binary alkali (alkaline)-earth silicate systems but cannot account for the more complex behavior at higher ionic potentials. Hudon and Baker adopted the Coulombic repulsion mechanism and built a selective-solute model [22,23]. In this model, the foreign cations (with different radii) are selectively trapped in the pentagonal apertures of the Si-O-Si network, which selectively screens their repulsion interaction and therefore results in a parabolic relationship between consolute temperature and ionic potential (see the dotted lines in Fig. 1).

These previous studies reveal a strong connection between melt structure and immiscibility extent in silicate systems, but a detailed understanding is still missing. On the one hand, the static structure conceived in the selective-solute model faces challenges in multicomposition silicate liquids, because the mixed-alkali effect will blur the definition of the localized cation traps [24,25]. On the other hand, atomic dynamics are rarely considered. This is problematic since the initiation and growth of the separated phase should be strongly coupled with the transport properties of the melts [26–28]. Therefore, a detailed explanation for the change in structure and dynamics during LLPS is needed for understanding the complex dependence of immiscibility extent on ionic potential. Here, considering the TiO_2-SiO_2 system, we perform first-principles

molecular dynamics calculations to track the structural rearrangements of the melt while crossing the immiscibility dome. This system was chosen due to the significant deviation of the consolute temperature in this system from the linear extrapolation for alkali (alkaline)-earth silicates [see Fig. 1(a)]. If considering the immiscibility region determined by Kirillova *et al.* as shown in Fig. 1(b), the consolute temperature of Ti^{4+} is lower [by the elliptical dashed box in Fig. 1(a)]. Furthermore, this system features a stable miscibility gap above the liquidus [14,29,30], avoiding a serious dynamic arrest in metastable immiscibility liquids (e.g., Al^{3+} and Ga^{3+} silicates) [14,19]. We find that the ionic potential has dual effects on the extent of liquid immiscibility: a higher ionic potential energetically favors the initiation of phase separation, while concurrently hindering its subsequent progression. Such dual effects were not considered in the previous structural models, which may contribute to understanding the origin of mesoscopic phase separation and structural heterogeneity in liquids and glasses [31,32].

II. COMPUTATIONAL METHODS

A. Simulation details

Ab initio molecular dynamics simulations (AIMD) were carried out based on density-functional theory using the Vienna *Ab initio* Simulation Package [33]. The interaction between the ionic core and valence electrons was treated with the projector augmented-wave method [34,35]. Both the generalized-gradient approximation and the Perdew-Burke-Ernzerhof formalism were employed for the exchange-correlation interaction [36,37]. The canonical ensemble (constant atomic number, volume, and temperature, *NVT*) was used. The plane-wave energy cutoff was set to be 400 eV, and the *k*-point mesh adopted for the Brillouin zone integrations was $1 \times 1 \times 1$ for all melt models. During the *NVT* simulations, the convergence criteria for both the total energy and the Hellmann-Feynman force were set as 10^{-5} eV and 0.01 eV/Å, respectively, to ensure sufficient accuracy.

In this work, the system considered had the composition $30TiO_2$-$70SiO_2$ because it is located in the LLPS compositional extent, according to the equilibrium phase diagram of the binary TiO_2-SiO_2 system [29]. Besides, the corresponding melt structures have been experimentally measured by synchrotron high-energy x-ray diffraction (HEXRD) [20]. We used a cubic cell containing 240 atoms (24 titanium, 56 silicon, and 160 oxygen) with periodic boundary conditions. To generate an initial configuration, a reverse Monte Carlo algorithm was applied to produce the atomic arrangement [38] according to our previous experimental results (structural correlation functions of the same composition melt at 2473 K). Subsequently, the initial configuration was rapidly relaxed at 5000 K for 2 ps (the total energy has converged). After equilibration at this temperature, we performed AIMD simulations at five preset temperatures: 3073, 2473, 2223, 1873, and 1273 K, which included high-temperature singlet liquids, two mixed liquids, and supercooled liquids, as shown in the SiO_2-TiO_2 phase diagram [see Fig. 1(b)].

Before the AIMD simulation, the edge length of the canonical ensemble at each temperature was tested carefully to ensure that the total pressure [the sum of the ideal gas part ($\rho k_B T$) and the external pressure] was less than 0.2 GPa, to recover the experimental pressure. The time step for the motion of the ions was set to be 3 fs, and the Nosé-Hoover thermostat was applied to control the temperature in the canonical ensemble [39]. Considering that the relaxation time in liquids strongly depends on the temperature, the length of the trajectories employed in the following for studying the structural and dynamic properties of the melts was $\geqslant$30 ps. This ensured that the diffusion region had been reached at each temperature [see the mean-square displacement in Figs. 4(a)–4(c)].

B. Static structure statistics

To characterize the change of local structure during phase separation, calculations were performed to acquire the two-body partial pair-correlation functions (PPCF) $g_{\alpha\beta}(r)$, the Faber-Ziman (FZ) form total structure factor $S(q)$, and the Ashcroft-Langreth (AL) form partial structure factors $S_{\alpha\beta}(q)$ [40,41]. Statistical averaging of $g_{\alpha\beta}(r)$ was achieved by sampling the final 10 000 structures (corresponding to 30 ps) as

$$g_{\alpha\beta}(r) = \frac{V}{N_\alpha(N_\alpha - \delta_{\alpha\beta})}\left\langle \sum_{i=1}^{N_\alpha}\sum_{j=1}^{N_\beta}\frac{1}{4\pi r^2}\delta(r - |\vec{r}_i - \vec{r}_j|)\right\rangle, \quad (1)$$

where V is the volume of the canonical ensemble. N_α and N_β are the number of atomic species of α and β, respectively δ is the Kronecker function; and $\vec{r}_i$ and $\vec{r}_j$ iterate over all coordinate vectors of both atoms. Operator $\langle \ldots \rangle$ means the spatial or time average. The FZ-form $S(q)$ was then computed from the Fourier transforms of the $g_{\alpha\beta}(r)$ functions,

$$S(q) = 1 + \sum_{\alpha,\ \beta=1}^{n} W_{\alpha\beta}\int_0^{r_{\max}} 4\pi\rho_0 r^2(g_{\alpha\beta}(r) - 1) \times \frac{\sin(qr)}{qr}\exp(-\gamma^2 r^2)dr, \quad (2)$$

where n is the number of atomic species in systems. $W_{\alpha\beta}$ is the weighting factor (for x ray or neutron), and ρ_0 is the average atomic number density. The expression $\exp(-\gamma^2 r^2)$ is a window function for the Fourier transforms, which was used to reduce the truncation effects caused by finite $r_{\max}$ ($L/2$, L is the edge length of the AIMD configuration) and limitation of periodic boundary conditions. The AL-form Si-Ti partial structure factors were computed using the definition

$$S_{\alpha\beta}(q) = \frac{1}{(N_\alpha N_\beta)^{1/2}}\left\langle \sum_{j=1}^{N_\alpha}\sum_{k=1}^{N_\beta}\exp[i\vec{q}\cdot(\vec{r}_j - \vec{r}_k)]\right\rangle, \quad (3)$$

where $\vec{q}$ is the discrete wave vector, which is calculated by $\vec{q} = 2\pi/L(n_x,\ n_y,\ n_z)$, and $n_x,\ n_y,\ n_z = 0,\ 1,\ 2,\ \ldots,\ n$. $\vec{r}_j$ and $\vec{r}_k$ iterate over all coordinate vectors of both atoms.

Except for atomic arrangement, the electronic structure was also analyzed using the Bader algorithm [42]. A total of ten configurations were uniformly taken out from the last 15 ps of AIMD ensembles in turn, on which geometrical optimization and charge-density calculation were then performed. The average effective charges (Q_{eff}) and volumes (V_{ion}) of Si,

Ti cations, and O anions in melts were finally determined by Voronoi segmentation of the charge-density grid.

C. Dynamical properties

Atomic movement upon LLPS was studied based on mean-squared displacement (MSD), Van Hove functions, and Debye-Waller factors [40,41]. As for a tagged particle of type α, MSD is calculated as

$$r_\alpha^2(t) = \frac{1}{N_\alpha}\sum_{i=1}^{N_\alpha}\langle|\vec{r}_i(t) - \vec{r}_i(0)|^2\rangle. \quad (4)$$

MSD represents the overall mobility of each type of particle, and it is therefore associated with the growth of the second phase during liquid immiscibility. To understand the detailed dynamical features of the separating particles during liquid immiscibility, we also calculated the self-part of the Van Hove functions as

$$G_s^\alpha(r,t) = \frac{1}{N_\alpha}\sum_{i=1}^{N_\alpha}\langle\delta(r - |\vec{r}_i(t) - \vec{r}_i(0)|)\rangle. \quad (5)$$

The Van Hove function describes the probability distribution of a distance r traveled by a particle undergoing Brownian motion over a certain time interval and thus provides the residence time before atomic heterogeneous microsegregation. To correlate atomic mobility with statistic structure in liquid immiscibility systems, the Debye-Waller factor $\langle\mu^2\rangle$ was used to describe the movement of a particle, which is defined as the MSD at an extremely small time interval [43].

III. RESULTS AND DISCUSSION

A. Microphase separation upon quenching

In binary glass-forming silicate liquids, the thermal immiscibility extent (quantified by consolute temperature) demonstrates a general increase with increasing the cation's ionic potential, as indicated by the empirical ExpAssoc curve fitted in Fig. 1. However, the variation of consolute temperature does not scale linearly with ionic potential; in addition, significant deviations from this general increment are observed as for some amphoteric cations (e.g., Al^{3+}, Ga^{3+}, and Ti^{4+}). Such a nonmonotonic and nonlinear relationship cannot be thoroughly explained by the previous phenomenological models, such as McGahay's model [21] and Hudon's selective-solute model [22,23].

We here seek to identify a unified structural mechanism to account for the nonmonotonic dependence of miscibility gap size on the ionic potential. To this end, we focus on the $30TiO_2$-$70SiO_2$ binary phase separation systems, where the existence of a stable immiscibility region above the liquidus [see Fig. 1(b)] has been demonstrated in experiments and thermodynamic calculation [14,29,30]. Figure 2(a) illustrates that the simulated FZ form $S(q)$ at three different temperatures agrees well with the existing experimental data [20]. However, it is worth noting that the first ripple appears at the higher-q side (decreased quasiperiodic length $2\pi/Q_1$) compared to the experimentally derived one. This shift may result from a finite-size effect and extreme cooling rates of the AIMD simulations, which leads to a poorly developed medium-order structure [44,45]. The intensity of the first diffraction peak of molten TiO_2-SiO_2 is notably weakened in comparison with that of molten silica, revealing that the well-developed Si-O-Si network may be disrupted due to the introduction of Ti–O bonds. According to AL form $S_{\alpha\beta}(q)$ calculation, the potential occurrence of compositional separation is confirmed. As shown in Figs. 2(b) and 2(c), the wave-vector limit ($q \to 0$) intensity in Si-Ti and Ti-Ti $S_{\alpha\beta}(q)$ patterns significantly enhanced or diminished at 2223 K, manifesting a composition fluctuation at this temperature [46]. From the equilibrium phase diagram of the TiO_2-SiO_2 binary system (see Fig. 1) [14,30], the temperature of 2223 K is within the stable miscibility gap ($2068 \sim 2468$K@$30TiO_2$-$70SiO_2$). This indicates that the AIMD simulations partially reproduce the initial liquid immiscibility behavior. In comparison, changes in wave-vector limit intensity are absent in Si-Si and three short-range order interactions (Si-O, Ti-O, and O-O), shown in Supplemental Material, Fig. S1 [47]. These results suggest that the phase separation in $70SiO_2$-$30TiO_2$ melt is mainly provoked by the compositional fluctuation of Ti, and the main body of the Si-O-Si network remains essentially unchanged during the initial stage of phase separation.

PPCF and coordination number (*CN*) analyses further confirm the heterogeneous structure developed through compositional separation. As shown in Figs. 2(d)–2(f) (for more details see Supplemental Material, Fig. S2 [47]), the PPCF around Ti varies strongly both above and below the liquid immiscibility temperature (2223 K). The insets of the figures show the accumulative correlation function of $4\pi\rho_0 r^2 g_{\alpha\beta}(r)$. It is seen that the nearest-neighboring Si-Ti pairs are well separated at 2223 K, whereas the Ti-Ti pair is highly enhanced at this temperature. Such changes in PPCF patterns agree with the observed variations in *CN* (Table I), as the *CN* of Si-Ti exhibits a minimum value at 2223 K in contrast to a maximal *CN* value of Ti-Ti pairs at the same temperature. These results suggest that localized aggregation of Ti-Ti pairs appears in the melt within the range of the miscibility gap. Such enhanced coordination between Ti particles corresponds to the formation of Ti-Ti clusters, as shown in Supplemental Material, Fig. S3 [47]; the average and/or maximum cluster size significantly increases when quenching the melt into the immiscibility temperature range (2223 and 1873 K). Precipitation of these Ti-Ti clusters may be initial precursors for the nucleation of the TiO_2-enriched is more appropriate droplet; therefore, AIMD simulations reproduce to some extent the microphase separation. In comparison with the structural changes around Ti, negligible coordination changes of Si-Si interactions and three short-range order (SRO) pairs, namely Si-O, Ti-O, and O-O, are observed [see Fig. 2(d) and Table I]. Moreover, well-distinguished phase-separation regions are not observed in the AIMD ensembles, unlike the case in classical MD simulations [10,48], which may be attributed to the smaller box size and shorter relaxation time in AIMD.

B. Coulomb repulsion driving Ti-Ti microscale clustering

AIMD simulations not only describe the atomic arrangement but also provide the electronic density distribution of the configuration that contributes to illustrating the influence of Coulomb repulsion on liquid immiscibility. According to the

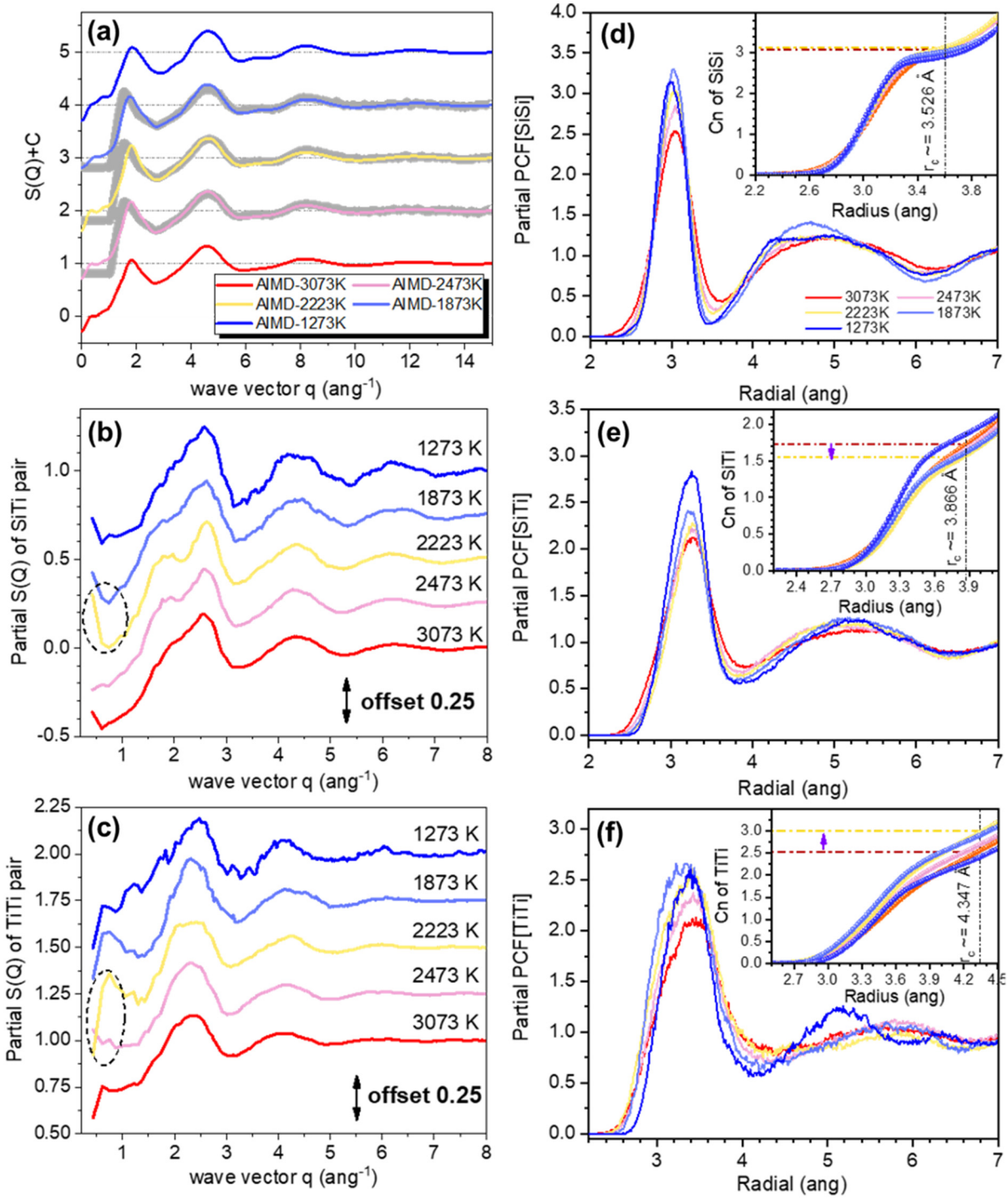

FIG. 2. Static structure evolution of molten TiO_2-SiO_2 upon LLPS. (a) AIMD simulated Faber-Ziman structure factors of molten TiO_2-SiO_2 at different temperatures. The curves are offset for clarity. The simulated results at three specific temperatures (i.e., 2473, 2273, and 1873 K) are compared with the corresponding experiment data (gray scatters) as measured by synchrotron HEXRD [20]. (b), (c) Partial AL-form structure factors of the (b) Si-Ti and (c) Ti-Ti pairs, as derived from AIMD ensembles according to $S(q)$ definition. (d)–(f) Partial pair-correlation functions of three cation-cation interactions (d) Si-Si, (e) Si-Ti, and (f) Ti-Ti. The insets show the accumulated coordination number as a function of radius.

Bader method [42], the average effective charges and atomic volumes of Si, Ti, and O atoms in the ensembles at different temperatures are obtained by the Voronoi segregation. As shown in Supplemental Material, Fig. S4 [47], the chemical valences of both Si and Ti cations increase as the temperature decreases and that of the anion O decreases to maintain charge neutrality. Meanwhile, the atomic volumes of Si and Ti cations notably decrease (see Supplemental Material, Fig. S5 [47]), reflecting that the distortion of valence electrons by thermal perturbation partially recovers as the temperature decreases.

TABLE I. Temperature-dependent coordination number of each atomic pair in the TiO_2-SiO_2 melts. The *CN* results were determined by integrating the first shell in the PPCF patterns or by connectivity analysis.

Temperature (K)	Si-Si pair $r_c = 3.53$ Å	Si-Ti pair $r_c = 3.87$ Å	Ti-Ti pair $r_c = 4.35$ Å	Si-O pair $r_c = 2.27$ Å	Ti-O pair $r_c = 2.73$ Å	O-O pair $r_c = 3.74$ Å
3073	2.99(3) | 2.937[a]	1.71(1) | 1.586[a]	2.55(3) | 2.156[a]	4.07(5)	5.02(1)	10.77(0)
2473	3.02(7) | 2.948[a]	1.64(8) | 1.516[a]	2.69(1) | 2.314[a]	4.06(0)	4.97(5)	10.87(5)
2223	3.05(5) | 2.960[a]	1.56(8) | 1.425[a]	2.96(5) | 2.511[a]	4.03(8)	5.00(7)	10.86(2)
1873	2.98(8) | 2.937[a]	1.60(8) | 1.508[a]	2.90(4) | 2.529[a]	4.04(3)	5.07(6)	10.80(7)
1273	2.86(4) | 2.803[a]	1.85(5) | 1.713[a]	2.40(7) | 2.062[a]	4.06(1)	5.04(8)	10.90(8)

[a]Numbers written in italics with a superscript "a" are calculated according to the connectivity, not the cutoff radius, where only these cations directedly connected by cation–oxygen bonds are considered as neighbor cations.

We then analyze the variations of the Coulomb potentials regarding the six partial ionic pairs $V_{\alpha\beta}(r)$ based on the derived chemical valences:

$$V_{\alpha\beta}(r) = \frac{1}{N_{\alpha\beta}}\left\langle \sum_{i=1}^{N_\alpha}\sum_{j=1}^{N_\beta}\frac{Q_iQ_j}{4\pi\varepsilon_r r_{ij}}\right\rangle, \tag{6}$$

where $N_{\alpha\beta}$ is the number of bonds between two particle types of α and β within a sphere shell centered on the ith ion of particle α and with the radius r_{ij} smaller than a specific cutoff [see Fig. 3(a)]; Q_i and Q_j are the chemical valences of the ith (particle α) and jth (particle β) ions. ε_r is the vacuum permittivity. Figures 3(b)–3(d) display the Coulomb potentials of three cation-cation interactions at different temperatures and cutoff radii. Only the Coulomb potential energy of Si-Ti pairs exhibits a relative decrease when crossing the miscibility gap (2223 K), and this decreasing trend shows a weak dependence on the cutoff radius. In contrast, the Coulomb potential energies of both Si-Si and Ti-Ti pairs increase after the microseparation of cations Si^{4+}/Ti^{4+} and the formation of aggregative Ti-Ti clusters [see Figs. 2(e) and 2(f) and Table I]. The reduction of the Coulomb potential energy implies that the Coulomb repulsion between Ti^{4+} cations and nearby Si^{4+} nodes positively contributes to the separation of the two cationic species, leading to the notable decrease of Si-Ti coordination number. Notably, such findings are inconsistent with previous understanding, where the Coulomb repulsion between poorly shielded cations (here, Ti^{4+}) was considered to be the main driving force for liquid immiscibility [21,22,49]. We have also analyzed the change of the Coulomb potentials of three SRO atomic pairs (see Supplemental Material, Fig. S6 [47]). Interestingly, a relative decrease of the Coulomb potential (absolute value) occurs between the first and the second coordination shell of Ti-O pairs at the stable immiscibility temperature (2223 K). This suggests that the stabilization of aggregative Ti-Ti clusters may be fulfilled by a connectivity change between adjacent [TiO_m] polyhedra, i.e., the rearrangement of Ti–O bonds, which compensate for the enhanced Coulomb repulsion among Ti-Ti bindings.

According to the pioneering work of Varshal *et al.*, the origin of liquid immiscibility was the incompatibility between structural groups of [SiO_4] tetrahedra and secondary cation-oxygen polyhedra [18]. Hudon *et al.* partially adopted this viewpoint in their selective-solute model and further proposed that these amphoteric cations (e.g., Ti^{4+} and Al^{3+}) in fourfold oxygen coordination will be better shielded than other oxygen coordination. This would reduce the repulsions between nearby cations and consequently lead to the nonmonotonic relevance of consolute temperature [22,23]. To test these hypotheses, we calculate the total forces acting on Ti^{4+} cations with different coordination numbers of oxygen. As shown in Supplemental Material, Fig. S7 [47], the total forces on Ti^{4+} cations with six- and fivefold oxygen are smaller than that of Ti^{4+} with fourfold oxygen coordination. In addition, these results are found to be independent of temperature. In other words, these high-coordinated (six- and fivefold) Ti^{4+} species are in more energy-balance positions compared with the four-coordinated Ti^{4+} cations, hence contradicting the inference of Hudon. Moreover, the total forces acting on Ti^{4+} cations also show a weak dependence on surrounding connectivity. As presented in Supplemental Material, Fig. S8 [47], the distribution of total forces on the central Ti^{4+} cation almost overlaps regardless of the number of connected cation-oxygen polyhedra. Coupling the localized Ti-Ti clusters formation and the Coulomb potentials analysis, the liquid immiscibility may be driven by the repulsion between Ti^{4+} cations and adjacent Si^{4+} network nodes over a large spatial scale. Furthermore, such Ti-Si repulsive interactions contradict the concept of the so-called structural incompatibility and thus question the validity of the previously established structural models concerning liquid immiscibility.

C. Slow dynamics hindering liquid immiscibility

Considering only the driving effect of the Coulomb repulsion on liquid immiscibility, as outlined in the model by McGahay *et al.* [21], it is plausible to infer that a larger ionic potential should correspond to a greater immiscibility extent. This, however, is not strictly consistent with the experimental observation of nonmonotonic evolution of consolute temperature (Fig. 1). Because most stages in the phase separation process (including nucleation and later growth of binodal droplet, the evolution of spinodal bands, etc.) are intimately related to the liquid transport properties [28,29,50], we next account for the dynamic effects. As shown in Fig. 4(a), the motion of ions in the simulation configurations has been determined by MSD calculations. The mobility of Ti^{4+} cations and O^{2-} anions are analogous, both of which are faster than that of

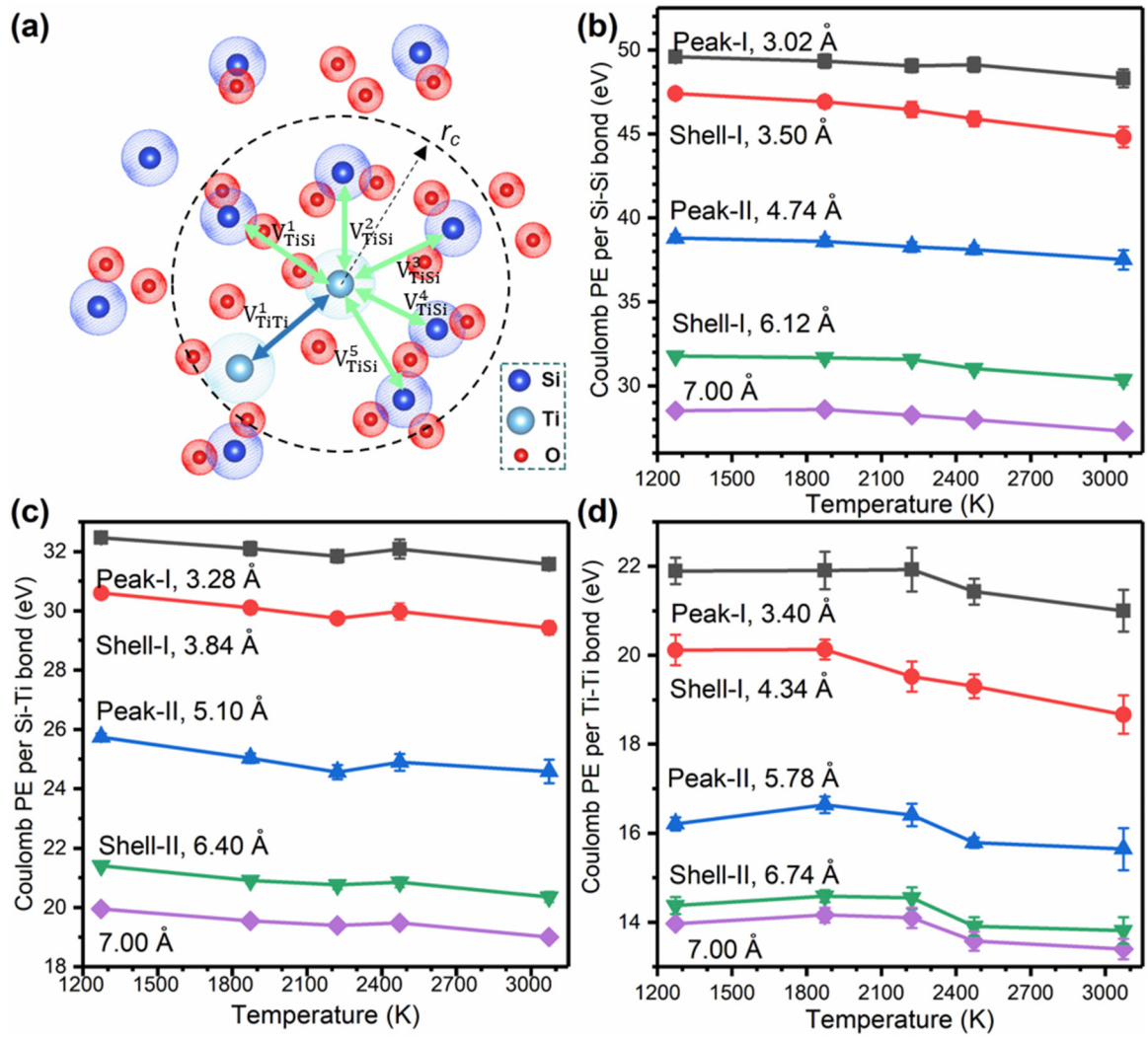

FIG. 3. Analysis of Coulomb repulsion interactions between the three cation-cation pairs. (a) Schematic diagram of Coulomb potential-energy accumulation for the Ti-Ti and Ti-Si pairs in a sphere shell with a radius r_c. (b)–(d) Dependence of the average Coulomb potential energy on temperatures and cutoff radii for (b) Si-Si, (c) Si-Ti, and (d) Ti-Ti pair. The cutoff radii are determined by corresponding PPCF patterns, from small to large ones, with the order being the first peak position, the first coordination shell, the second peak position, the second coordination shell, and approximately half of the simulation configuration.

Si^{4+} cations. This partly accounts for why the local structure around Ti^{4+} cations notably changes upon the microphase separation, while the Si-Si connectivity remains unchanged (see Fig. 2 and Table I). Double-logarithm plots of the MSD vs time for Ti^{4+} and Si^{4+} show a similar trend [Figs. 4(b) and 4(c)]. The ending times (∼0.25 ps) of the ballistic regime for the patterns of the two cations are almost identical, but significantly different from that of alkali-silicate systems [46]. This suggests that Ti and alkali cations occupy different interstices in the Si-O-Si network. At higher temperatures (e.g., 3000 and 2473 K), the ballistic regime is almost immediately connected by a diffusive regime. But, at the lowest temperature (1273 K), this connection is interrupted by a relatively flat region (the so-called cage effect), as it is often seen in an undercooled liquid [51].

By fitting the MSD in the diffusive regime through the Einstein-Stokes relation [Eq. (7)], we can calculate the self-diffusion coefficient D_α of the two cations,

$$D_\alpha = \lim_{t\to\infty} \frac{r_\alpha^2(t)}{6t}. \tag{7}$$

As presented in the Arrhenius plot of the D_α dependence on temperature [Fig. 4(d)], the D_α of Ti is larger than that of Si, indicating diffusion of Ti^{4+} ions is faster than that of Si^{4+} ions. Furthermore, based on log D_α vs $1/T$ plot, the activation energy for diffusion of Ti and Si can be determined by linear regression. Intriguingly, we find that the activation energy E_A for the diffusion of Ti increases from 0.56 ± 0.06 eV (pure titania) to 1.28 ± 0.14 eV ($30TiO_2$-$70SiO_2$), while that of Si decreases from 5.18 ± 0.08 eV (pure silica) to 1.68 ± 0.26 eV ($30TiO_2$-$70SiO_2$). That is, the mobility decreases for Ti^{4+} while it increases for Si^{4+} compared with that in the molten SiO_2 [52], illustrating the component-mixing effect on the atomic dynamics. Such changes in dynamics are common in

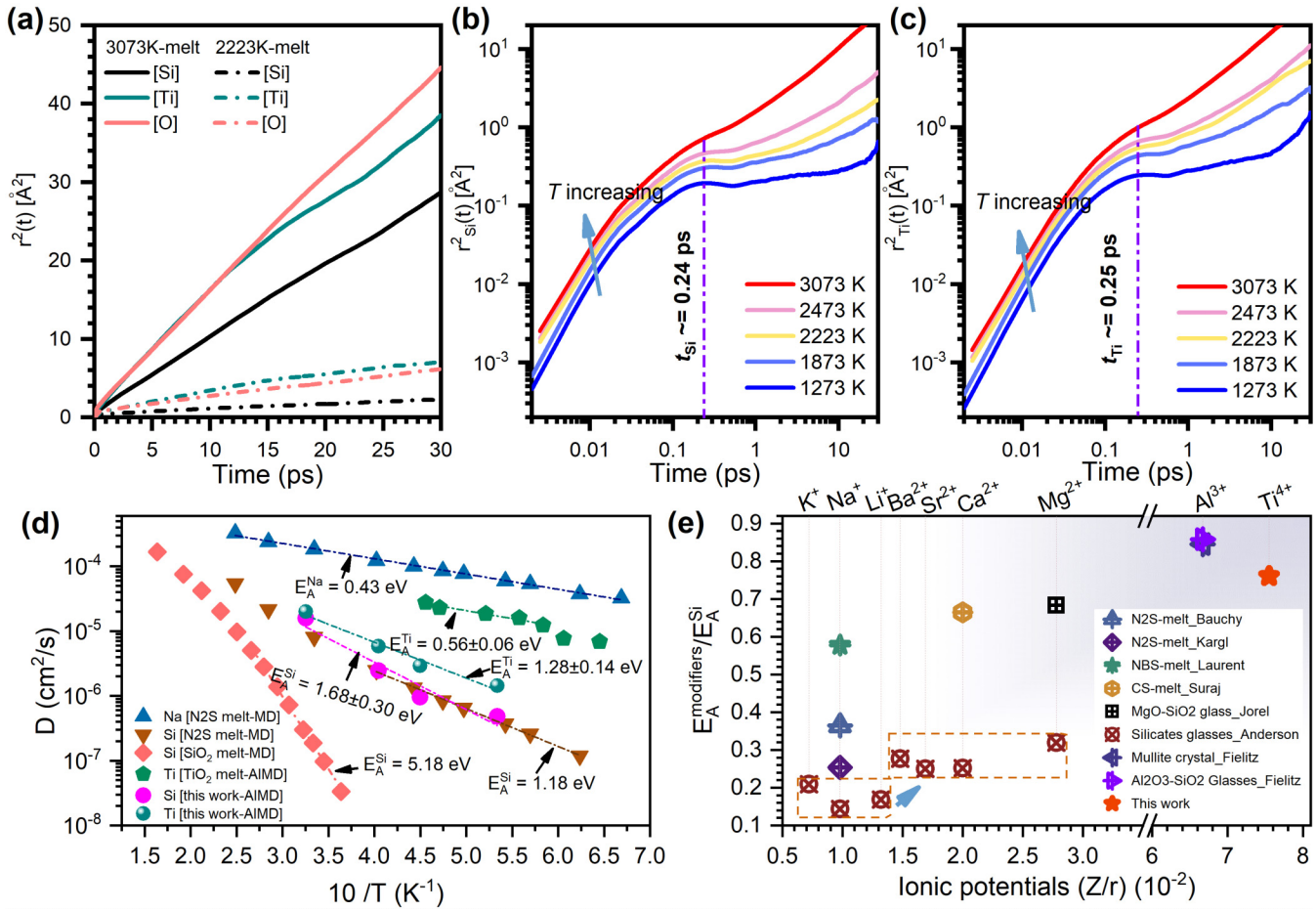

FIG. 4. Dynamic changes of TiO_2-SiO_2 liquids upon cooling across LLPS region, and the comparison of ionic transport behaviors concerning different secondary cations in silicate liquid/glass. (a) Comparison of the mean-square displacement [MSD, $r^2(t)$] curves for Si, Ti, and O ions at two specific temperatures. (b), (c) Double-logarithm plot of the partial MSD for (b) Si^{4+} and (c) Ti^{4+} cations for the five simulated temperatures. (d) Calculated self-diffusion constants of cations (Si^{4+} and Ti^{4+}) in TiO_2-SiO_2 liquid immiscibility systems as a function of the inverse temperature. The data are compared with that of pure silica [52], titania (our unpublished data), and Na_2O-$2SiO_2$ melts [53]. The activation energy for diffusion is extracted from fitting the Arrhenius equation of D_α to the data. (e) Ratio of the activation energy of different cations to that of Si^{4+} in silicate melts or glasses [46,53–58]. The data for silicate glasses under consideration have been normalized by dividing the E_α of alkali (alkali-earth cations by that of pure silica (5.18 eV).

silicate systems, as manifested in Fig. 4(d) [53]. The activation energy of Si^{4+} has decreased from 5.18 eV (pure silica) to as low as 1.18 eV (Na_2O-$2SiO_2$ melts), whereas the D_α of Na^+ is an order of magnitude larger than that of Ti^{4+} [53]. The variation of dynamics is assumed to be correlated with the ionic potential of the secondary cation, as the transport properties of silicate melts and glasses are primarily influenced by the polymerization/depolymerization of the Si-O-Si network. This process is closely correlated with the concentration of nonbridging oxygen, which is partially dependent on the ionic potential of the secondary cation.

To illustrate the relationship between the transport properties of cations and their ionic potentials, we define a dimensionless ratio E_A^α/E_A^{Si} (where α represents different cations species) to qualitatively describe the relative height of the energy barrier in the transport process. We assume that the larger the value of this ratio, the more similar the local diffusion path between the cations and Si^{4+} should be, implying stronger interactions among the cations and the surrounding network. Figure 4(e) shows E_A^α/E_A^{Si} vs ionic potential for several silicate systems [46,53–58]. We find that the E_A^α/E_A^{Si} values show an overall increase with increasing ionic potentials. Interestingly, Al^{3+} exhibits the highest E_A^α/E_A^{Si} ratio that corresponds to a most sluggish movement of the cation, and hence it undergoes a most notable decrease in consolute temperature [see Fig. 1(a)]. Considering the arguments presented above, the increased ionic potential slows down the cationic migration across the surrounding network, consequently being unfavorable for the evolution of microphase separation.

D. Correlation between atomic dynamics and local structure

To further elucidate the linkage between atomic dynamics and structural changes during liquid immiscibility, the self-part of the Van Hove functions $G_s^\alpha(r, t)$ regarding the Si, Ti, and O species (at 2223 K) is calculated [Fig. 5(a)]. These curves from left to right correspond to increasing time intervals (0.015 to 30 ps). For short time intervals ($t < 0.24$ ps),

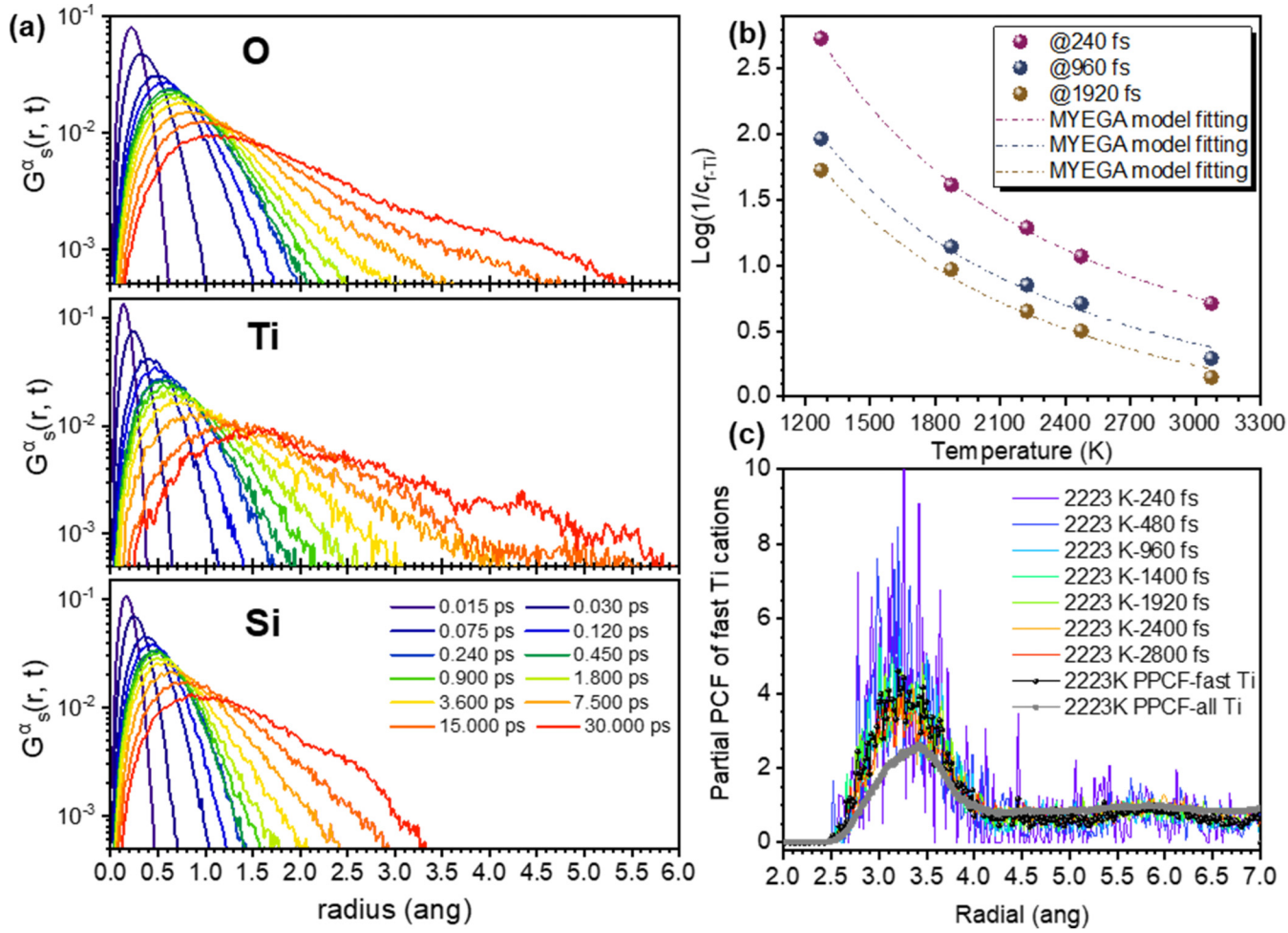

FIG. 5. The dynamic heterogeneity of Ti particles. (a) Self-part of the Van Hove correlation function $G_s^{\alpha}(r,\ t)$ for α = Si, Ti, and O at 2223 K and for different time intervals. (b) Relationship between the reciprocal of fast-Ti content and temperature, as determined for three specific observation times. The data are fitted with a MYEGA form equation (dashed lines). (c) Partial pair-correlation function of fast-moving Ti cations, including comparison with the PPCF of all Ti cations.

the $G_s^{\alpha}(r,\ t)$ patterns are analogous to Gaussian distributions, being in line with the ballistic motion regime [see Figs. 4(b) and 4(c)]. For longer time intervals, the $G_s^{\alpha}(r,\ t)$ gradually deviates from the Gaussian distributions, reflecting the presence of dynamic heterogeneity [59]. According to the $G_s^{\alpha}(r,\ t)$ results, Ti^{4+} cations exhibit higher mobility than that of Si^{4+}, as Ti^{4+} diffuses for a longer distance at the same time interval. At 2223 K, the movements of the Si^{4+} cations are limited to the first shell of the Si-Si pair within 30 ps, illustrating that the network reorganization during microphase separation is mainly fulfilled by position exchange between adjacent cation-oxygen polyhedra. That is, the formation of aggregative Ti-Ti clusters is attributed to the migration of Ti^{4+} across the network. Moreover, a shoulder is observed at around 2.75 Å (30 ps, Si), i.e., around the nearest-neighbor distance of Si-Si [see Fig. 2(d)]. Hence, the shoulder could be a signature of hoppinglike motion [46,52]. The motion of Ti^{4+} and O^{2-} ions exhibits diffusion-like behavior at 2223 K for all time intervals. Only at an even lower temperature (1273 K), as shown in Supplemental Material, Fig. S9 [47], an obvious shoulder is found at around 2 Å (20 ps, Ti), indicating the diffusion of Ti depends on hoppinglike motion. Additionally, in the supercooled liquid state (1223 K), the motion of Si^{4+} is limited within a [SiO_4] tetrahedra, reflecting that the Si-O-Si network has been almost dynamically arrested. Both this frozen network and the constrained Ti^{4+} diffusion explain why the localized Ti-Ti clusters disappear at 1223 K (see Table I).

To form these aggregative Ti-Ti clusters, the minimum steric hindrance is estimated to be around 1.5 Å, corresponding to the gap between the first coordination shell and the second peak position in Ti-Ti PPCF patterns [see Fig. 2(f)]. If these Ti particles move more than 1.5 Å within a defining time interval, we define them as "fast Ti." Thus, the fluctuation of fast-Ti particles reflects the microscopic dynamical changes during the microphase separation. The fraction of fast Ti in the ensembles is then calculated at different temperatures and different time intervals (see Supplemental Material, Figs. S10(a) and S10(b) [47]). We find that the content of fast Ti increases with both temperature and observation time. With decreasing temperature, the fast-Ti content exponentially decreases, indicating that the viscosity of liquid notably increases as the

mobility of the microscopic particles is inversely proportional to the macroscopic viscosity (according to the Einstein-Stokes relation). The temperature dependence of the reciprocal of fast-Ti content is displayed in Fig. 5(b), The temperature dependence of the reciprocal of fast-Ti content is displayed in Fig. 5(b), and the data were fitted by the Mauro-Yue-Ellison-Gupta-Allan (MYEGA) equation [60].

$$\log\left(\frac{1}{C_{f-\mathrm{Ti}}}\right) = C + (12 - C)\frac{A}{T}\exp\left[\left(\frac{B}{15} - 1\right)\left(\frac{A}{T} - 1\right)\right], \tag{8}$$

where $C_{f-\mathrm{Ti}}$ is the fraction of fast Ti, T is the temperature, and A, B, and C are fitting parameters. C refers to the high-temperature limit of fast Ti particles [61]. The good fitting suggests that the LLPS process may not involve any dynamical anomalies, in contrast to the discontinuous structural change (see Fig. 2 and Table I). That is, the structural reorganization and dynamic behavior during liquid immiscibility might be decoupled. Figure 5(c) shows the PPCF between these fast-Ti particles, meaning that the intensity of the first peak is notably higher than that of the PPCF pattern derived from all Ti particles. This indicates that the interaction between fast-Ti species is strengthened and in turn an entangled movement when Ti particles percolate through the Si-O-Si network to form aggregative Ti-Ti clusters.

From the above dynamical analysis, it is evident that the formation of the microaggregative Ti-Ti clusters mainly results from Ti^{4+} cations' diffusion-like movements. However, the dynamic behaviors of Ti^{4+} cations appear to be independent of the discontinuous structural changes within microphase separation. This phenomenon is different from that observed previously in metastable glasses and supercooling liquids, where the dynamic arrest and heterogeneity of microscopic particles are closely correlated with their local structure [59,62,63]. Such decoupling between dynamics and structure calls for an updated understanding of the correlation between local structure and atomic dynamics in liquid immiscibility. Figures 6(a)–6(f) show the relationship between Ti^{4+} cations' mobility (donating as Debye-Waller factor, μ^2 [43]) and their local coordinated number at the immiscibility temperature (2223 K). The two-dimensional frequency distribution F (CN, μ^2) is obtained by counting the number of Ti particles in the range of $\mu^2 + \Delta\mu^2$ with a certain coordination number CN. The F (CN, μ^2) presents a unipolar peak distribution [see Figs. 6(a), 6(c), and 6(e)], where the peak position approximately corresponds to the local maxima of the $G_s^{\alpha}(r,\ t)$ patterns [compared to Fig. 5(a)] and the coordination species distribution around Ti particles (see Supplemental Material, Fig. S11 [47]). According to the two-dimensional frequency distributions, the probable distribution of Ti^{4+} mobility with a specific coordination number $F^{\theta}(\mu^2)|_{CN=n}$ is normalized as

$$F^{\theta}(\mu^2)|_{CN=n} = \frac{F(CN,\ \mu^2)|_{CN=n}}{x|_{CN=n}}, \tag{9}$$

where $x|_{CN=n}$ is the fraction of motifs with n coordination number. All the results of normalized $F^{\theta}(\mu^2)|_{CN=n}$ [see Figs. 6(b), 6(d), and 6(f)] reveal significant overlap for the same coordinating pairs. Moreover, this finding also remains valid in the high-temperature homogeneous liquids (3073 K, shown in Supplemental Material, Fig. S12 [47]). Hence, the mobility of Ti ions exhibits a weak correlation with their surrounding local structure, which explains the decoupling between dynamics and structural changes during microphase separation. Our results thus question the validity of Hudon's selective-solute model, according to which the dynamics of amphoteric cations (including Ti^{4+}) are markedly slowed down when they occupy some specific interstices in the Si-O-Si network [23]. Furthermore, this microscopic transport scenario in titania-bearing silicate melt also should be distinct from that in alkali-silicate melts, where the formation of alkali-rich channels at the medium-range order scale is believed to enable fast motion of the alkali cations [63,64].

While no significant correlation between the mobility of Ti particles and their surrounding network structure can be found, enhanced interactions exist among the fast Ti, as shown in Fig. 5(c). To decipher the origin of these strong collective dynamics, the dynamic linkage between Ti^{4+} and their nearest-neighbor oxygen is analyzed. As presented in Fig. 6(g), the dynamical correlation distribution suggests these faster-moving Ti^{4+} particles tend to correspond to these faster-moving oxygens. This dynamic correlation of Ti^{4+} particles with neighboring oxygens is better represented by statistically averaging the Debye-Waller factor over different time intervals, as done in Fig. 6(h). Within a certain bounded length (r^{cri}), the increased μ^2 of Ti^{4+} particles positively correlates with the increased averaged μ^2 of its coordination oxygens, demonstrating that the motions of these two types of particles are tightly coupled in the bounded length.

We further analyze the spatial range of dynamic coupling around Ti particles [Fig. 6(i)]. The dynamic correlation is weakened as the cutoff radius increases, as the slopes of the curves gradually decrease. However, there exists a noticeable abrupt change within the range of 3–3.5 Å, mainly corresponding to the first coordination shells of Ti-Si and Ti-Ti interactions [see Figs. 2(e) and 2(f)]. Based on the above analysis, it is evident that the mobility of Ti^{4+} weakly correlates with the surrounding static network structure, leading to the decoupling between continuous dynamics and discontinuous structural evolution during liquid immiscibility. In contrast, the mobility of Ti^{4+} particles is strongly correlated with their surrounding atoms, especially with the coordinating oxygens. This suggests that the formation of aggregative Ti-Ti pairs during microphase separation is driven by the collective movement of Ti^{4+}-centered clusters that are organized by mutual constraints between ions.

E. Linkage between atomic dynamics and topological rigidity of chemical bindings

According to the results of the activation energy for diffusion [Figs. 4(d) and 4(e)], slow dynamics of amphoteric cations (Ti^{4+} and Al^{3+}) hinder their transport in the surrounding Si-O-Si network due to higher energy barrier for diffusion. This is unfavorable for the evolution of liquid immiscibility. The energy barrier, which traps the motions of particles, manifests itself as the effective binding strength (interatomic rigidity) within the particles and must be related to the ionic potentials [43]. To estimate the interatomic rigidity around Ti^{4+}, topological rigidity theory provides a feasible strategy

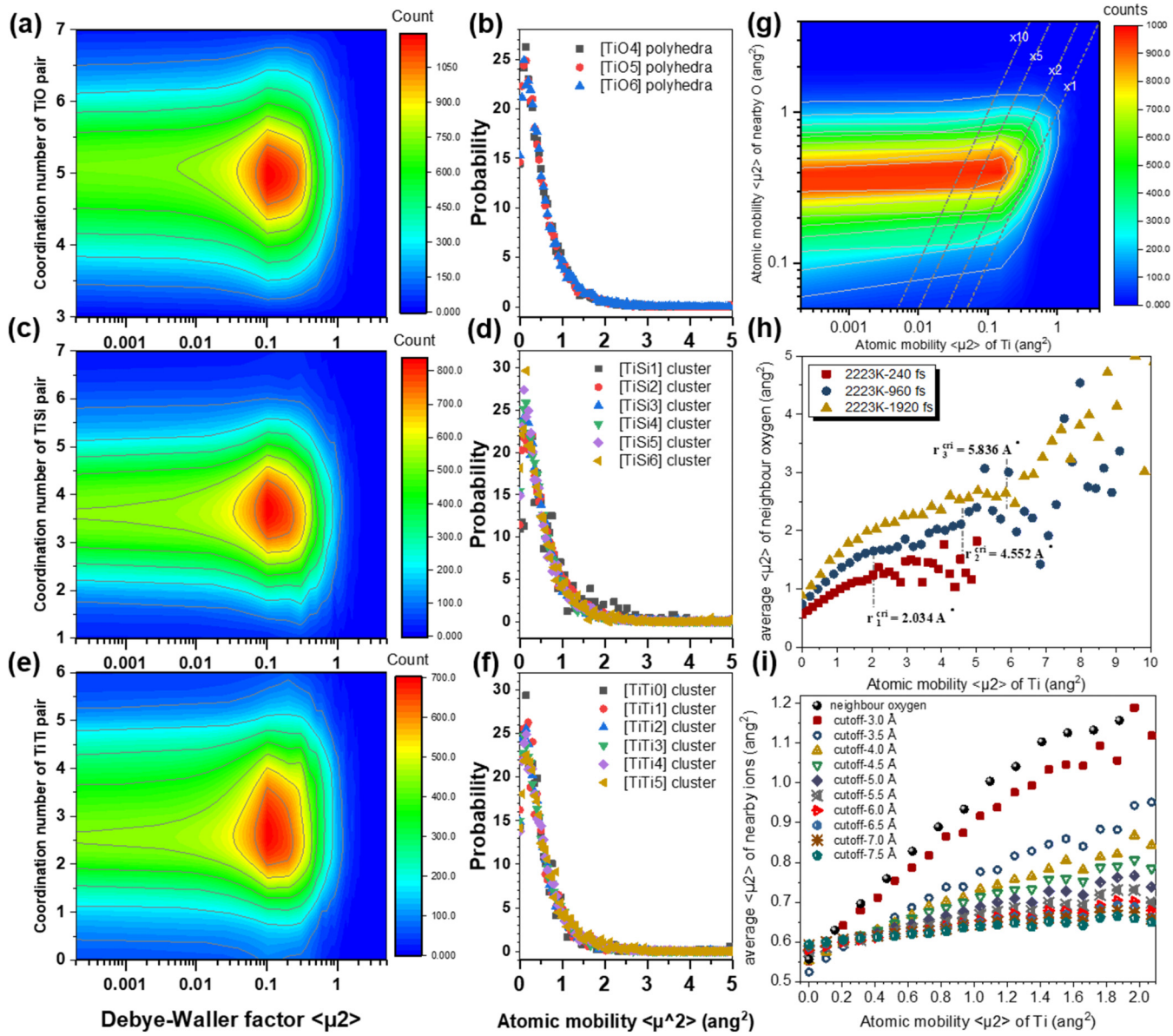

FIG. 6. Correlation between dynamic behavior of Ti particles and their surrounding local structure. Relationship between mobility (240-ps Debye-Waller factor μ^2, 2223 K melt) of Ti^{4+} cations and their local coordination structures: (a), (b) Ti-O pair, (c), (d) Ti-Si pair, and (e), (f) Ti-Ti pair. (g) Dependence of the Ti^{4+} mobility on that of the nearest-neighbor O^{2-} anions, which corresponds to the 240-ps interval μ^2 of the 2223 K melt ensembles. The gray dashed lines labeled with ×1, ×2, ×5, and ×10 correspond, respectively, to contours at 1, 2, 5, and 10 times the Ti^{4+} cations' mobility (μ^2). (h) Dynamic correlation between Ti^{4+} and its nearest-neighbor oxygen. The motions are expressed as the average μ^2 over different time intervals. (i) Linkage between the mobility of Ti^{4+} (μ^2 − 240 fs) and the average mobility of vicinity ions for different spatial ranges around them.

[65]. According to the definition by Phillips *et al.*, there are two-body (radial) and three-body (angular) constraints imposed on pairwise atoms. Here, only angular constraints are considered, because the radial constraints are determined by the number of nearest-neighboring oxygens ($CN/2$, where CN is the coordination number of oxygen) [66], and the latter has a weak correlation with the mobility of Ti particles [Figs. 2, 6(a), and 6(b)]. Angular constraints are counted using the approach proposed by Bauchy *et al.* [67,68]. As shown in Fig. 7(a), 21 sets of O–Ti–O partial bond-angle distributions (PBADs) are calculated and their respective standard deviation σ is derived [Fig. 7(b)]. The standard deviation provides an estimation of the strength of the angular restoring forces. Significantly smaller σ values are observed in six sets of PBADs, suggesting that the six partial O–Ti–O bond angles ($\widehat{O_1TiO_2}$, $\widehat{O_1TiO_3}$, $\widehat{O_1TiO_4}$, $\widehat{O_2TiO_3}$, $\widehat{O_2TiO_4}$, and $\widehat{O_3TiO_4}$) feature relatively low angular excursion: this is, relatively strong angular constraints [67,69]. Moreover, the six angle components with smaller σ distribution also illustrate that only the 4 oxygens (O_1, O_2, O_3, and O_4) nearest to Ti are in relatively rigid positions. Intriguingly, these findings might explain why certain spectroscopic studies (e.g., Raman or

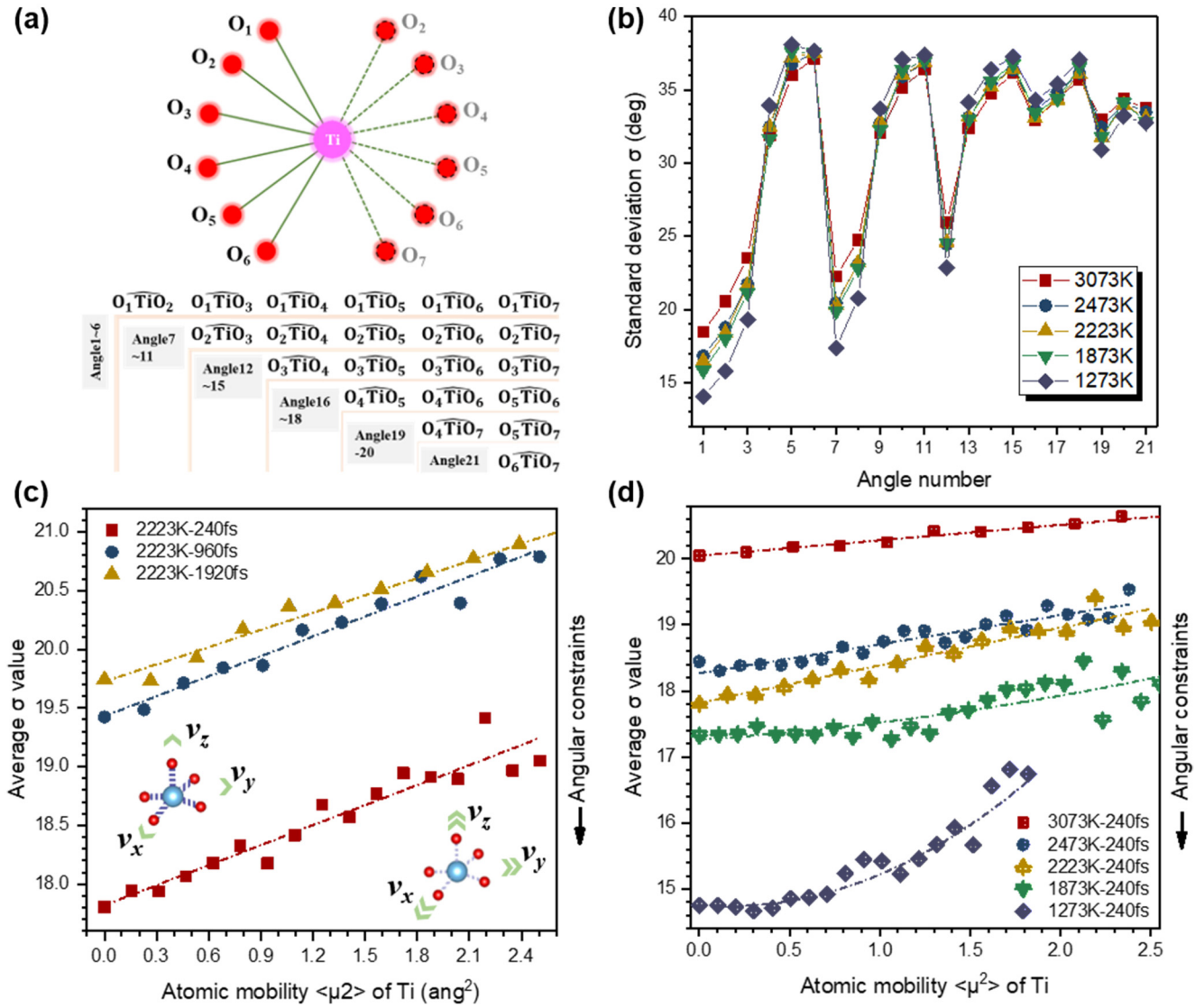

FIG. 7. Linkage between Ti^{4+} transport in the silicate network and its surrounding topological rigidity. (a) Determination of angular constraints surrounding Ti^{4+} cations according to the partial bond-angle distributions (PBADs). Seven first-neighbor oxygens are identified, corresponding to 21 sets of PBADs. The notation of O_i (subscript i range from 1 to 7) represents the sequence of distance from neighbor oxygen to center Ti^{4+} cations. (b) Standard deviations of the 21 sets of varying bond angles, named as σ [shown in panel (a)] as a function of the angle number, with a large (small) σ value representing broken (intact) constraints. (c) Relationship between the mobility of Ti particles (μ^2@ 2223 K, with three different time intervals) and its surrounding angular constraints. The angular constraints are calculated by averaging the six minima σ values in panel (b). (d) Relationship between the mobility of Ti particles (μ^2@ 240 ps, under different temperatures) and its surrounding angular constraints.

infrared spectroscopy) conducted on titanate-bearing melts have exclusively identified the presence of [TiO_4] polyhedra [70]. These fourfold motifs are intact for a longer lifetime due to the smaller angular excursion, providing sufficient acquisition time for the vibration modes. The average of the six smallest σ values is used as the estimation of the total angular constraints; thus, a smaller average σ value indicates a larger angular constraint.

The correlation between the Debye-Waller factor μ^2 of Ti^{4+} particles and the total angular constraints is shown in Fig. 7(c), which exhibits a linear relation, implying a strong connection between the mobility of Ti^{4+} particles and the O–Ti–O bond-angle excursion (average σ) in the liquid immiscibility gap (2223 K). The fast-moving Ti^{4+} particles are prone to have relatively weak angular constraints and vice versa. Importantly, the observed linear relationship remains independent of the sampling time, confirming a robust association between ionic dynamics and the topological angular constraints. Furthermore, the angular constraints vs ionic dynamics relationships are investigated at different temperatures [Fig. 7(d)]. The linear relationship remains in three equilibrium liquids (3073, 2473, and 2223 K), but the relation gradually becomes nonlinear in the supercooled liquids (1873 and 1273 K). Interestingly, there exists a dynamical threshold (i.e., critical mobility) for these undercooling liquids, above which the increased Ti particle mobility is accompanied by a reduction in angular constraints. This phenomenon is reminiscent of the so-called caging effect. Moreover, upon cooling,

the extreme angular constraints denoted as the limit σ of the static Ti particles ($\mu^2 \to 0$), are enhanced (σ decreases) due to the freezing of the thermal vibration of the particles. Especially at 1223 K, the limit σ reaches a range of 14.8–17, comparable to that of [$SiSe_4$] and [$GeSe_4$] tetrahedra units in prototypical chalcogenide network glasses [67]. Due to a large ionic potential of Ti^{4+}, the angular constraints within [TiO_m] polyhedra are quite strong, resulting in highly correlated migration of Ti particles and their neighbor oxygen [Fig. 6(i)].

We also compared the angular constraints of Ti with those of Na. A much larger σ value of O-Na-O PBADs (far-weaker angular constraints surrounding Na) has been reported [68], which contributes to a smooth penetration of Na through the Si-O-Si network. These calculations of topological constraints further clarify the decoupling of dynamics and local structure. As the angular constraints around Ti particles can mainly be ascribed to the four nearest oxygens, the mobility of Ti^{4+} cations confined in three prominent [TiO_m] ($m = 4$, 5, and 6) polyhedra are consistent [see Figs. 6(a) and 6(b)]. Additionally, the mobility of Ti particles shows a weak correlation not only with the number of surrounding cation-oxygen polyhedra [see Figs. 6(c)–6(f)] but also with the connectivity between these adjacent polyhedra (network connectivity analysis is provided in Supplemental Material [47]). According to Figs. S13 and S14 [47], the Ti–O–M PBADs (M = Ti and Si) and sharing modes in different Ti-centered coordinating clusters are distinct, while the mobility of Ti^{4+} in these clusters is almost the same [see Figs. 6(c)–6(f)]. Such weak dynamic-structure coupling may originate from the weak angular constraints of Ti–O–M (M = Ti and Si) bond angles (see Supplemental Material, Fig. S15). There are no striking differences observed in the Ti–O–M angular constraints among various complexed cations-cations clusters, further implying that the second shell structure around Ti^{4+} particles (i.e., cations-cations connectivity) is highly floppy [71], thereby not confining the Ti particles' motion.

IV. CONCLUSIONS

We have investigated the structural response and dynamic behavior of the TiO_2-SiO_2 immiscibility system to decipher the mechanism of the nonmonotonic extent of immiscibility observed in silicate melts. The atomic ensembles constructed by AIMD simulations effectively reproduce the heterogeneous microsegregation among Ti^{4+} cations. The separation process of Si and Ti is accompanied by a decrease in the Coulomb potential of Si-Ti interactions, which conversely corresponds to an increase in the Coulomb potential of Si-Si and Ti-Ti interactions. Our results question the conventional consensus that the separation of different cations results from the Coulomb repulsion between poorly shielded cations (here, Ti^{4+}). Additionally, the dynamic behavior also differs from the prediction of the classical selective-solute model. The atomic motion shows little correlation with their local coordination structures, and no pronounced changes corresponding to the heterogeneously structural rearrangement in the microphase separation.

The ionic potential is proposed to be a key descriptor for predicting the liquid immiscibility extent. The increase in ionic potential enhances the driving force (the Coulomb potential) for phase separation, due to the reinforced repulsion between modifiers and adjacent Si^{4+} nodes. However, the increased ionic potential also dynamically decreases the immiscibility propensity, since the strengthened binding between cations and neighboring oxygens leads to enhanced topological angular constraints around the cations, which consequently slow down their diffusion. Overall, the above dual effects of ionic potential account for the nonmonotonic immiscibility extent in silicate melts. Our work provides an atomic-scale picture of LLPS, contributing to developing a unified, structure-thermodynamic consistent model for the liquid immiscibility phenomenon in oxide systems. The findings have implications for the dynamic and structural heterogeneity in supercooled liquids, which is a general phenomenon to be understood in glass science.

ACKNOWLEDGMENTS

This work was supported by the National Natural Science Foundation of China-Key Programme (52234010), and National Natural Science Foundation of China-Outstanding Young Scholars (52325407). X.G. and M.M.S. acknowledge support for a MSCA Postdoctoral Fellowship (101062110) from the Horizon Europe Framework Programme.

X.G., together with Q.H., formulated the research project; X.G. and M.M.S. finalized the data analysis as well as wrote the manuscript; X.G. and P.L. performed the AIMD simulations and discussed the output data; X.G. and C.S. processed the HEXRD data and discussed the discrepancies of $S(Q)$ patterns between HEXRD and AIMD; and T.D., Z.L., Y.Y., W.L., F.Y., J.Q., and J.L. discussed the data, revised the manuscript, and provided instructive suggestions.

[1] T. Keller, F. Tornos, J. M. Hanchar, D. K. Pietruszka, A. Soldati, D. B. Dingwell, and J. Suckale, Genetic model of the El Laco magnetite-apatite deposits by extrusion of iron-rich melt, Nat. Commun. **13**, 6114 (2022).

[2] A. F. Wallace, L. O. Hedges, A. Fernandez-Martinez, P. Raiteri, J. D. Gale, G. A. Waychunas, S. Whitelam, J. F. Banfield, and J. J. De Yoreo, Microscopic evidence for liquid-liquid separation in supersaturated $CaCO_3$ solutions, Science **341**, 885 (2013).

[3] S. Alberti, A. Gladfelter, and T. Mittag, Considerations and challenges in studying liquid-liquid phase separation and biomolecular condensates, Cell **176**, 419 (2019).

[4] L. Fu, B. Wang, S. K. M. Sathyanath, J. Chang, J. Yu, K. Leifer, H. Engqvist, Q. Li, and W. Xia, Microstructure of rapidly-quenched ZrO_2-SiO_2 glass-ceramics fabricated by container-less aerodynamic levitation technology, J. Am. Ceram. Soc. **106**, 2635 (2022).

[5] C. Wang, X. Liu, I. Ohnuma, R. Kainuma, and K. Ishida, Formation of immiscible alloy powders with egg-type microstructure, Science **297**, 990 (2002).

[6] P. F. James, Liquid-phase separation in glass-forming systems, J. Mater. Sci. **10**, 1802 (1975).

[7] O. Dargaud, L. Cormier, N. Menguy, G. Patriarche, and G. Calas, Mesoscopic scale description of nucleation processes in glasses, Appl. Phys. Lett. **99**, 021904 (2011).

[8] Q. Zhang, L. R. Jensen, R. E. Youngman, T. To, T. Du, M. Bauchy, and M. M. Smedskjaer, Influence of phase separation microstructure on the mechanical properties of transparent modifier-free glasses, J. Non-Cryst. Solids **595**, 121806 (2022).

[9] K. Sun, D. Tan, X. Fang, X. Xia, D. Lin, J. Song, Y. Lin, Z. Liu, M. Gu, Y. Yue, and J. Qiu, Three-dimensional direct lithography of stable perovskite nanocrystals in glass, Science **375**, 307 (2022).

[10] Z. Li, C. Chen, W. Shen, D. Zhou, L. R. Jensen, X. Qiao, J. Ren, J. Du, Y. Zhang, J. Qiu, and Y. Yue, The transformation from translucent into transparent rare earth ions doped oxyfluoride glass-ceramics with enhanced luminescence, Adv. Opt. Mater. **10**, 2102713 (2022).

[11] D. H. Kim, W. T. Kim, E. S. Park, N. Mattern, and J. Eckert, Phase separation in metallic glasses, Prog. Mater. Sci. **58**, 1103 (2013).

[12] S. S. Kim and T. H. Sanders, Thermodynamic modeling of the miscibility gaps and the metastable liquidi in the MgO-SiO_2, CaO-SiO_2, and SrO-SiO_2 systems, J. Am. Ceram. Soc. **82**, 1901 (1999).

[13] P. C. Hess, Upper and lower critical points: Thermodynamic constraints on the solution properties of silicate melts, Geochim. Cosmochim. Acta **60**, 2365 (1996).

[14] M. Kirschen, C. DeCapitani, F. Millot, J.-C. Rifflet, and J.-P. Coutures, Immiscible silicate liquids in the system SiO_2-TiO_2-Al_2O_3, Eur. J. Mineral. **11**, 427 (1999).

[15] B. Warren and A. Pincus, Atomic consideration of immiscibility in glass systems, J. Am. Ceram. Soc. **23**, 301 (1940).

[16] E. M. Levin and S. Block, Structural interpretation of immiscibility in oxide systems: I. Analysis and calculation of immiscibility, J. Am. Ceram. Soc. **40**, 95 (1957).

[17] F. Glasser, I. Warshaw, and R. Roy, Liquid immiscibility in silicate systems, Phys. Chem. Glasses **1**, 39 (1960).

[18] B. Varshal, A structural model of immiscibility of silicate glass-forming melts, Glass. Phys. Chem. **19**, 218 (1993).

[19] S. K. Wilke, C. J. Benmore, V. Menon, J. Ilavsky, A. Rezikyan, R. E. Youngman, M. P. Carson, and R. Weber, Revisiting metastable immiscibility in SiO_2-Al_2O_3: Structure and phase separation of supercooled liquids and glasses, J. Am. Ceram. Soc. **106**, 2820 (2023).

[20] C. Zhang, X. Ge, Q. Hu, F. Yang, P. Lai, C. Shi, W. Lu, and J. Li, Atomic scale structural analysis of liquid immiscibility in binary silicate melt: A case of SiO_2-TiO_2 system, J. Mater. Sci. Technol. **53**, 53 (2020).

[21] V. McGahay and M. Tomozawa, The origin of phase separation in silicate melts and glasses, J. Non-Cryst. Solids **109**, 27 (1989).

[22] P. Hudon and D. R. Baker, The nature of phase separation in binary oxide melts and glasses. I. Silicate systems, J. Non-Cryst. Solids **303**, 299 (2002).

[23] P. Hudon and D. R. Baker, The nature of phase separation in binary oxide melts and glasses. II. Selective solution mechanism, J. Non-Cryst. Solids **303**, 346 (2002).

[24] H. Sreenivasan, P. Kinnunen, E. Adesanya, M. Patanen, A. M. Kantola, V.-V. Telkki, M. Huttula, W. Cao, J. L. Provis, and M. Illikainen, Field strength of network-modifying cation dictates the structure of (Na-Mg) aluminosilicate glasses, Front. Mater. **7**, 267 (2020).

[25] Y. Onodera, Y. Takimoto, H. Hijiya, T. Taniguchi, S. Urata, S. Inaba, S. Fujita, I. Obayashi, Y. Hiraoka, and S. Kohara, Origin of the mixed alkali effect in silicate glass, NPG. Asia. Mater. **11**, 75 (2019).

[26] Y. Gueguen, P. Houizot, F. Célarié, M. Chen, A. Hirata, Y. Tan, M. Allix, S. Chenu, C. Roux-Langlois, and T. Rouxel, Structure and viscosity of phase-separated BaO-SiO_2 glasses, J. Am. Ceram. Soc. **100**, 1982 (2017).

[27] D. Bouttes, O. Lambert, C. Claireaux, W. Woelffel, D. Dalmas, E. Gouillart, P. Lhuissier, L. Salvo, E. Boller, and D. Vandembroucq, Hydrodynamic coarsening in phase-separated silicate melts, Acta Mater. **92**, 233 (2015).

[28] S. Schuller, O. Pinet, and B. Penelon, Liquid-liquid phase separation process in borosilicate liquids enriched in molybdenum and phosphorus oxides, J. Am. Ceram. Soc. **94**, 447 (2011).

[29] S. A. Kirillova, V. I. Almjashev, and V. V. Gusarov, Phase relationships in the SiO_2-TiO_2 system, Russ. J. Inorg. Chem. **56**, 1464 (2011).

[30] C. DeCapitani and M. Kirschen, A generalized multicomponent excess function with application to immiscible liquids in the system CaO-SiO_2-TiO_2, Geochim. Cosmochim. Acta **62**, 3753 (1998).

[31] Y. Yue, Revealing the nature of glass by the hyperquenching-annealing-calorimetry approach, J. Non-Cryst. Solids: X **14**, 100099 (2022).

[32] H. Tanaka, Bond orientational order in liquids: Towards a unified description of water-like anomalies, liquid-liquid transition, glass transition, and crystallization: Bond orientational order in liquids, Eur. Phys. J. E **35**, 113 (2012).

[33] G. Kresse and J. Furthmüller, Efficiency of ab-initio total energy calculations for metals and semiconductors using a plane-wave basis set, Comput. Mater. Sci. **6**, 15 (1996).

[34] P. E. Blochl, Projector augmented-wave method, Phys. Rev. B.: Condens. Matter **50**, 17953 (1994).

[35] J. P. Perdew and Y. Wang, Accurate and simple analytic representation of the electron-gas correlation energy, Phys. Rev. B.: Condens Matter. **45**, 13244 (1992).

[36] G. Kresse and D. Joubert, From ultrasoft pseudopotentials to the projector augmented-wave method, Phys. Rev. B **59**, 1758 (1999).

[37] J. P. Perdew, K. Burke, and M. Ernzerhof, Generalized gradient approximation made simple, Phys. Rev. Lett. **77**, 3865 (1996).

[38] O. Gereben and L. Pusztai, RMC_POT: A computer code for reverse Monte Carlo modeling the structure of disordered systems containing molecules of arbitrary complexity, J. Comput. Chem. **33**, 2285 (2012).

[39] S. Nosé, A unified formulation of the constant temperature molecular dynamics methods, J. Chem. Phys. **81**, 511 (1984).

[40] K. Binder and W. Kob, *Glassy Materials and Disordered Solids: An Introduction to Their Statistical Mechanics* (World Scientific. Singapore, 2011).

[41] J. P. Hansen and I. R. McDonald, *Theory of Simple Liquids: With Applications to Soft Matter* (Academic Press. London, 2013).

[42] W. Tang, E. Sanville, and G. Henkelman, A grid-based Bader analysis algorithm without lattice bias, J. Phys.: Condens. Matter. **21**, 084204 (2009).

[43] F. W. Starr, S. Sastry, J. F. Douglas, and S. C. Glotzer, What do we learn from the local geometry of glass-forming liquids?, Phys. Rev. Lett. **89**, 125501 (2002).

[44] C. Massobrio, J. Du, M. Bernasconi, and P. S. Salmon, *Molecular Dynamics Simulations of Disordered Materials* (Springer International Publishing, Cham, 2015).

[45] L. Deng and J. Du, Effects of system size and cooling rate on the structure and properties of sodium borosilicate glasses from molecular dynamics simulations, J. Chem. Phys. **148**, 024504 (2018).

[46] L. Pedesseau, S. Ispas, and W. Kob, First-principles study of a sodium borosilicate glass-former. I. The liquid state, Phys. Rev. B **91**, 134201 (2015).

[47] See Supplemental Material at http://link.aps.org/supplemental/10.1103/PhysRevB.109.174215 for additional structural details, including AL-form $S(Q)$ and PPCF of three SRO pairs; the evolution of aggregative Ti-Ti clusters; more detailed results from electronic structure analysis, such as variation of chemical valence and atomic volume, and the dependence of Coulomb potential energy of three SRO pairs on temperatures and cutoffs; the association of total force applied on centering Ti^{4+} cations with their local coordinating environments; additional self-part Van Hove functions for Si/Ti/O for high-temperature (3073 K) and undercooling melts; variations of fast-Ti contents with temperatures and observation time; the distribution of three types of cation-cation coordinating clusters; the relationship between the mobility of Ti^{4+} cations and their local coordination structures at 3073 K; network connectivity analysis of the phase-separated liquid (2223 K); and the angular constraints of Ti-O-M (M is Ti or Si) bond angles.

[48] X. Bidault, S. Chaussedent, and W. Blanc, A simple transferable adaptive potential to study phase separation in large-scale xMgO-(1-x)SiO_2 binary glasses, J. Chem. Phys. **143**, 154501 (2015).

[49] A. B. Thompson, M. Aerts, and A. C. Hack, Liquid immiscibility in silicate melts and related systems, Rev. Mineral. Geochem. **65**, 99 (2007).

[50] D. Bouttes, E. Gouillart, and D. Vandembroucq, Topological symmetry breaking in viscous coarsening, Phys. Rev. Lett. **117**, 145702 (2016).

[51] M. Micoulaut, Relaxation and physical aging in network glasses: A review, Rep. Prog. Phys. **79**, 066504 (2016).

[52] J. Horbach, W. Kob, and K. Binder, Structural and dynamical properties of sodium silicate melts: An investigation by molecular dynamics computer simulation, Chem. Geol. **174**, 87 (2001).

[53] M. Bauchy, B. Guillot, M. Micoulaut, and N. Sator, Viscosity and viscosity anomalies of model silicates and magmas: A numerical investigation, Chem. Geol. **346**, 47 (2013).

[54] S. K. Bajgain, D. B. Ghosh, and B. B. Karki, First-principles simulations of CaO and $CaSiO_3$ liquids: Structure, thermodynamics and diffusion, Phys. Chem. Miner. **42**, 393 (2015).

[55] F. Kargl, A. Meyer, M. M. Koza, and H. Schober, Formation of channels for fast-ion diffusion in alkali silicate melts: A quasielastic neutron scattering study, Phys. Rev. B **74**, 014304 (2006).

[56] J. Fourmont, W. Blanc, D. Guichaoua, and S. Chaussedent, Phase-separated Ca and Mg-based nanoparticles in SiO_2 glass investigated by molecular dynamics simulations, Sci. Rep. **12**, 11959 (2022).

[57] P. Fielitz and G. Borchardt, Self-diffusion of the constituent elements in alpha-alumina, mullite and aluminosilicate glasses, Diffus. Fundam. **8**, 80 (2016).

[58] O. Anderson and D. Stuart, Calculation of activation energy of ionic conductivity in silica glasses by classical methods, J. Am. Ceram. Soc. **37**, 573 (1954).

[59] C. P. Royall and S. R. Williams, The role of local structure in dynamical arrest, Phys. Rep. **560**, 1 (2015).

[60] J. C. Mauro, Y. Yue, A. J. Ellison, P. K. Gupta, and D. C. Allan, Viscosity of glass-forming liquids, Proc. Natl. Acad. Sci. USA **106**, 19780 (2009).

[61] Q. Zheng and J. C. Mauro, Viscosity of glass-forming systems, J. Am. Ceram. Soc. **100**, 6 (2017).

[62] D. R. Neuville and C. Le Losq, Link between medium and long-range order and macroscopic properties of silicate glasses and melts, Rev. Mineral. Geochem. **87**, 105 (2022).

[63] A. Meyer, J. Horbach, W. Kob, F. Kargl, and H. Schober, Channel formation and intermediate range order in sodium silicate melts and glasses, Phys. Rev. Lett. **93**, 027801 (2004).

[64] G. N. Greaves and S. Sen, Inorganic glasses, glass-forming liquids and amorphizing solids, Adv. Phys. **56**, 1 (2007).

[65] J. C. Phillips and M. Thorpe, Constraint theory, vector percolation and glass formation, Solid. State. Commun. **53**, 699 (1985).

[66] J. C. Mauro, Topological constraint theory of glass, Am. Ceram. Soc. Bull. **90**, 31 (2011).

[67] M. Bauchy, M. Micoulaut, M. Celino, S. Le Roux, M. Boero, and C. Massobrio, Angular rigidity in tetrahedral network glasses with changing composition, Phys. Rev. B **84**, 054201 (2011).

[68] M. Bauchy and M. Micoulaut, Atomic scale foundation of temperature-dependent bonding constraints in network glasses and liquids, J. Non-Cryst. Solids **357**, 2530 (2011).

[69] M. Bauchy and M. Micoulaut, Transport anomalies and adaptative pressure-dependent topological constraints in tetrahedral liquids: Evidence for a reversibility window analogue, Phys. Rev. Lett. **110**, 095501 (2013).

[70] P. T. Sarjeant and R. Roy, Ti^{4+} coordination in glasses in RO-TiO_2 systems, J. Am. Ceram. Soc. **52**, 57 (1969).

[71] X. Ge, P. Lai, C. Shi, X. Xu, J. Wang, T. Du, M. M. Smedskjær, D. Yang, F. Yang, W. Lu, J. Qin, J. Li, and Q. Hu, Unconventional floppy network structures in titanate glasses, Acta Mater. **253**, 118953 (2023).